

Gaseous Dynamical Friction: a Numerical Study of Extended Perturbers

B. Morton,¹★ S. Khochfar,¹ J. Oñorbe,²

¹*Institute for Astronomy, Royal Observatory, Edinburgh EH9 3HJ, UK*

²*Facultad de Física, Universidad de Sevilla, Sevilla, Spain*

Accepted XXX. Received YYY; in original form ZZZ

ABSTRACT

The process of momentum and energy transfer from a massive body moving through a background medium, known as dynamical friction (DF), is key to our understanding of many astrophysical systems. We present a series of high-resolution simulations of gaseous DF using Lagrangian meshless finite mass hydrodynamics solvers in the state-of-the-art multiphysics code *Gizmo*, the moving-mesh MUSCL scheme in *Arepo*, and the PPM solver in the *Enzo* adaptive mesh refinement code. We setup simulations of extended perturbers moving with Mach $0.2 \leq \mathcal{M} \leq 3$ and investigate at which radial distances from the perturber they recover the linear point-mass perturber solutions for the DF drag force, the radial structure of the wake, and their time evolution. The various different solvers agree with each other and we find that the wake structure is recovered, at the 5% level, beyond $r_{\min} = 4r_s$, with r_s being the softening scale of the Plummer perturber. The drag force from the gravitationally induced wake is recovered, at this level, beyond this radius. Numerical convergence is reached where the effective initial spatial resolution is $0.2r_s$. This is roughly equivalent to 5 cells per gravitational softening scale in a grid-based code. The value of r_{\min} provides a natural way to compare different codes and allows us to estimate the difference in DF force that will be experienced. Our results further predict that semianalytic models using the point-mass linear DF estimate from Ostriker (1999) will overestimate the DF forces on the extended perturber by as much as 25%, for Mach numbers close to 1. Finally, we show that DF is typically in the linear regime for most subhaloes in hosting haloes $< 10^{11} M_{\odot}$ but non-linear in more massive host haloes.

Key words: methods: numerical – hydrodynamics

1 INTRODUCTION

As a massive object moves through some background medium, gravitational interactions build an over-density in the wake of the massive traveller. Momentum and energy are transferred from this massive perturber to the surrounding medium. This process is known as dynamical friction (DF) and is key to our understanding of the evolution of a number of astronomical systems. These systems cover very different mass and length scales. DF drives processes from galaxy clusters (El-Zant et al. 2004; Kim et al. 2005; Adhikari et al. 2016), to satellite galaxies orbiting within their host halo (Zhao 2004; Fujii et al. 2006; Ogiya & Burkert 2016), supermassive black hole formation (Beckmann et al. 2018), compact object binaries and mergers (Just et al. 2010; Dosopoulou & Antonini 2017; Tagawa et al. 2018), galaxy mergers (Khochfar & Burkert 2001), and planets within disks (Teyssandier et al. 2012).

In the case of galaxy clusters, DF plays a key role in driving the accretion of substructure. Hierarchical collapse, within the standard Λ CDM cosmological model, predicts the presence of large num-

bers of low mass subhaloes within higher mass hosts. The number density of satellites found in simulations follows a power law, with a slope of approximately -2 , predicting a steep increase in the number density of satellites going to lower masses (Springel et al. 2008). These structures will experience both *collisionless* and *collisional*, or gaseous, DF. These emerge as the sub-structure moves within extended dark matter (DM) and circumgalactic medium (CGM) of the host. DF provides a mechanism by which the substructure sheds angular momentum and energy, allowing it to merge with the central galaxy (Boylan-Kolchin et al. 2008; Khochfar & Ostriker 2008). In this way, DF drives the build-up of structure in a cold dark matter (CDM) cosmology. These mergers are a key driver of the evolution of galaxies, providing fuel for star formation and disrupting galactic structures (Barnes & Hernquist 1996; Beckman et al. 2008; Robaina et al. 2010; Khochfar et al. 2011; Somerville & Davé 2015). Gaseous DF is particularly pronounced at high redshifts, where halo gas-mass fractions are highest (Daddi et al. 2010; Tacconi et al. 2010). The exact number, and spatial distribution, of DM substructures varies with different cosmological models. Large scale cosmological simulations are a key tool in testing these models, and the comparison of simulated and observed DM substructure

★ E-mail: morton@roe.ac.uk

is currently a key challenge for Λ CDM (Weisz & Boylan-Kolchin 2019).

The structure of the overdense wake can be separated into two distinct contributions, one from a collisionless medium, such as background stars or cold dark matter, and one from a collisional component, typically baryonic gas. The additional pressure forces present in collisional media result in significant differences in the retarding drag force, when compared to the collisionless case (Ostriker 1999). This is most pronounced for Mach numbers close to $\mathcal{M} = 1$, when the combination of perturber mass and extent produce a wake that remains in the linear regime¹ As the induced wake becomes increasingly non-linear, the gaseous DF drag force decreases (Kim & Kim 2009) (referred to as KK09 when mentioned directly). The complex structure of gravitationally induced wake has previously been studied using both analytic (Just & Kegel 1990; Ostriker 1999; Namouni 2010) and numerical approaches (Sánchez-Salcedo & Brandenburg 1999, 2001; Kim & Kim 2007; Kim & Kim 2009; Thun et al. 2016; Park & Bogdanović 2017; Suzuguchi et al. 2024; Bernal & Sánchez-Salcedo 2013)(BS13). With a simplified, adiabatic, single-phase, ideal-gas background, the growth of the wake is effectively scale-free, allowing the analytic predictions to be applied across scales.

The analytic collisionless solution is found by calculating a sum of two body interactions, integrated over all time, between the perturber and an infinite background medium (Chandrasekhar 1943). The analytical solution to the collisional case can be obtained in the linear regime, producing an approximation of the structure of the wake using linear perturbation theory (Just & Kegel 1990; Ostriker 1999). Within this linear approximation, the collisional drag force is significantly higher for perturbers moving with Mach numbers $0.7 < \mathcal{M} < 2$. A similar trend is also observed, in numerical simulations, for low-mass, extended, perturbers (Sánchez-Salcedo & Brandenburg 1999; Kim & Kim 2009; Bernal & Sánchez-Salcedo 2013). Importantly, however, the analytic prediction for the wake's structure is only accurate in the linear to slightly non-linear regime. This is typically achieved at distances larger than a characteristic size of the perturber r_s . We will use the analytic solution in the linear regime as the benchmark and will therefore compare the numerical simulations to predictions on scales larger than r_s .

The above works produce fitted values for r_{\min} , the minimum radius of the retarding force integral (Ostriker 1999), beyond which the numerical results match the analytic prediction. This allows one to compare predictions from different solvers, with regards to each other, and to the point mass solution. It is important to note that a match in force does not necessarily mean that the numerical and analytic wakes have the identical wake structure, since forces are calculated by integrating over the wake and as such can average out variations in the density structure. However, the wake structure at scales larger than r_{\min} follows closely that of a point mass, and r_{\min} can therefore be seen as the distance at which the simulations agree with the linear point-mass predictions. Sánchez-Salcedo & Brandenburg (1999) find that $r_{\min} = 2.25r_s$ accurately produces the predicted forces. BS13 estimate the value of r_{\min} using the position of the maximum density in the wake produced by a Plummer sphere, as opposed to the position of a point mass, finding a value consistent with the Sánchez-Salcedo & Brandenburg (1999) result. KK09, on the other hand, find a Mach dependent prescription, with $r_{\min} =$

$0.35\mathcal{M}^{0.6}r_s$ and argue that the difference between their result and previous ones is caused by differences in resolution and equation of state. BS13 address this suggestion, and find no difference in results between isothermal and adiabatic equations of state, or with resolution. They use the $r_{\min} = 2.25r_s$ fit, but also explore a Mach dependent fit, resulting in $r_{\min} = 1.5\mathcal{M}^{0.6}r_s$. BS13 conclude that it is only applicable at later times $t > 130t_c$ for supersonic perturbers. Both fits discussed by BS13 use a value significantly larger than that found by KK09, which has a dramatic effect on the absolute value of the drag force from the wake. BS13 note that the KK09 fit can produce a force as much as a factor of two larger than their own. The value of r_{\min} is extremely important, when considering the drag force, as it determines over which radii the drag force is accurately described by the linear analytic prediction and what forces different solvers produce for the same setup. It is therefore worth exploring a 'best fit' value for r_{\min} , across Mach numbers, by comparing the force produced in a simulated wake to the analytic prediction, for different lower radial limits. The analytic prescription can be extended numerically for more extreme mass perturbers, where large regions of the wake are no longer described by the linear wake, as is done in KK09 and BS13. The simulation work, in this regime, does not produce a consistent or simple prediction for the nonlinear wake.

More complex scenarios, such as those that include more physical processes, have also been studied, such as extended perturbers (Furlanetto & Loeb 2002; Kim & Kim 2009), rigid perturbers that experience both gravitational drag, and the drag from physical collisions with the surrounding medium (Thun et al. 2016), as well as perturbers on orbital trajectories (Sánchez-Salcedo & Brandenburg 2001; Kim & Kim 2007), and the effect of radiative feedback from an accreting black hole on the drag force (Toyouchi et al. 2020).

Despite the studies mentioned above, the ability of modern cosmological simulation codes to accurately capture the effects of gaseous DF, in its full cosmological context, has not been studied in detail. Capturing the effects of DF requires modelling the hydrodynamic response, as well as the purely gravitational effects. The specifics of the hydrodynamic problem makes it difficult for traditional hydro solvers to model accurately (Tittley et al. 2001). The extended gaseous structure is highly asymmetric in certain directions, a challenge for standard Eulerian grid-based methods, which make use of a variety of hydrodynamics solvers (Teysier 2002; Bryan et al. 2014; Morton et al. 2023). Basic Lagrangian particle-based methods, such as SPH (Gingold & Monaghan 1977), can better handle irregular density structures, but are less accurate at handling hydrodynamic instabilities (Agertz et al. 2007).

In the last decade, a new hybrid class of methods has been developed, utilising moving unstructured mesh approaches that attempt to merge the advantages of the two. They aim to provide the instability and shock capture efficiency of grid-based methods with the natural resolution adaptation of particle methods. Within astrophysics, these methods are still relatively new, although several established codes have emerged (Springel 2010; Duffell & MacFadyen 2011; Hopkins 2015; Duffell 2016; Springel et al. 2020). These have been shown to be generally competitive with the established multi-physics simulation codes (Wadsley et al. 2004; Springel 2005; Bryan et al. 2014; Gonnet 2014; Menon et al. 2015; Wadsley et al. 2017). They are ideal for studying the effects of DF, as their natural resolution and stability to shocks should allow them to capture the sharp cone of the supersonic wakes. However, idealised DF studies have not been attempted with modern moving-mesh methods.

The impact of DF is a topic of significant ongoing study in

¹ Here the linear regime refers to wakes where the increase in density factor $\alpha = \rho/\rho_0 - 1$ is less than one, at a given radius, based on ones specific setup.

many different scenarios. The drag force prescription from [Ostriker \(1999\)](#) is frequently applied as a subgrid model, or in analytic and semi-analytic studies ([Tagawa et al. 2018](#); [Antoni et al. 2019](#); [Bonetti et al. 2020](#); [Bortolas et al. 2021](#); [Ma et al. 2021](#)). Comparing numerical results of extended perturbers to the analytic point mass predictions will allow to estimate the error on DF force calculations in such models. In our study, we will focus on the actual emergence of this perturbation within hydrodynamic simulations, looking to understand the impact of resolution on the outcome. The effective resolution available to capture the gravitationally induced wake self-consistently, even in the most cutting-edge simulations, is often low. In other words, a relatively small number of particles, or cells, resolve the mass and length scales of the wake. To arrive at robust conclusions from cosmological simulations of galaxy formation, it is therefore necessary to understand the impact very low mass and length resolutions might have on the formation and evolution of the dynamical friction wake.

In this work, we present a set of idealised, state-of-the-art, three-dimensional gravo-hydrodynamic simulations of massive Plummer spheres, embedded within a uniform region of adiabatic gas moving with some velocity. In [Section 2](#) we summarise the relevant analytic predictions. [Section 3](#) describes the numerical setup that we use, and [4](#) contains our results, showing the predicted wake, the force across a range of Mach numbers, and the impact of resolution. In [Section 5](#) we discuss these results, and examine the implication of our findings for dynamical friction experienced by dark-matter subhaloes in a cosmological context.

2 ANALYTIC SOLUTION TO DYNAMICAL FRICTION IN GASEOUS MEDIA

In contrast to dynamical friction in a collision-less medium, pressure gradients within a gaseous medium introduce additional forces on the evolving gas. These forces lead to the formation of structure within the overdense wake. The time-dependent form of this structure can be derived using linear perturbation theory to model the density perturbation as an expanding density wave ([Ostriker 1999](#)).

2.1 Linear Wake

Using linear perturbation theory, [Ostriker \(1999\)](#)² produced an analytic prediction for the force of DF felt by a point mass perturber M_p , moving at constant velocity V_0 in the z -direction through a gaseous medium with infinite uniform density ρ_0 , where the gas does not have self-gravity. The medium has sound speed c_s , and the perturber moves with Mach number $\mathcal{M} \equiv V_0/c_s$. The resultant analytic prescription for the density distribution of the induced wake, $\rho = \rho_0(1 + \alpha)$, described by the over-density $\alpha(s, R, t)$, is

$$\alpha = \frac{GM_p/c_s^2}{[s^2 + R^2(1 - \mathcal{M}^2)]^{1/2}} \times \begin{cases} 1 & \text{if } R^2 + z^2 < (c_s t)^2 \\ 2 & \text{if } \mathcal{M} > 1, R^2 + z^2 > (c_s t)^2, \\ & s/R < -(\mathcal{M}^2 - 1)^{1/2}, z > c_s t/\mathcal{M} \\ 0 & \text{otherwise} \end{cases} \quad (1)$$

where $s = z - vt$ is the distance from the perturber along the direction of travel and R is the cylindrical radius. Formally, this distribution diverges as the spherical radius $r \rightarrow 0$. However, the solution should

be valid in the linear regime. This part of the wake is approximately defined by $r \gtrsim r_{\min}$ with $GM_p/c_s^2 \lesssim r_{\min} \lesssim (V_0 - c_s)t$. The lower limit ensures that all parts of the wake included in this analysis are within the linear regime, while the upper limit requires that the wake extends beyond r_{\min} itself.

Still following [Ostriker \(1999\)](#), and by integrating over this overdense wake from r_{\min} to the edge of the wake, using

$$F_{\text{DF}} = 2\pi GM_p \rho_0 \int \int R \frac{\alpha(t)s}{(s^2 + R^2)^{3/2}} ds dR, \quad (2)$$

the drag force created by new mass distribution asymmetry takes the form

$$F_{\text{DF}} = -\frac{4\pi(GM_p)^2 \rho_0}{V_0^2} I. \quad (3)$$

The parameter I represents the integral over the over-density, divided by the collisionless solution, and is the factor by which the DF force differs from the purely collisionless case. It depends on Mach number, with

$$I_{\text{sub}} = \frac{1}{2} \ln \left(\frac{1 + \mathcal{M}}{1 - \mathcal{M}} \right) - \mathcal{M} \quad (4)$$

for the subsonic perturbers, and

$$I_{\text{super}} = \frac{1}{2} \ln \left(\frac{\mathcal{M} + 1}{\mathcal{M} - 1} \right) + \ln \left(\frac{\mathcal{M} - 1}{r_{\min}/c_s t} \right) \quad (5)$$

for the supersonic perturbers. The parameter I as a function of the Mach number is shown in [Figure 1](#). This result is only accurate when all regions of the wake included in the force calculation remain linear. In other words, this solution assumes $\alpha \lesssim 1$. The force predicted by this approach is greater than the equivalent collisionless force, for a range of Mach numbers $0 \lesssim \mathcal{M} \lesssim 3$ (see [Figure 3](#) of [Ostriker \(1999\)](#)). The largest difference comes when we are close to $\mathcal{M} = 1$, where the collisional prediction is undefined. We use the standard definitions for sub-sonic $v_0 < c_s$, $\mathcal{M} < 1$, and super-sonic $v_0 > c_s$, $\mathcal{M} > 1$, with the transition point at $v_0 = c_s$, $\mathcal{M} = 1$. It should be noted that the collisional drag force deviates by a factor of a few from the pure collisionless case. This increases with time, as the collisional solution is time dependent, while the collisionless is not.

When this prediction is tested numerically, the condition for the wake to remain linear $\alpha < 1$ can be parameterised using the dimensionless parameter A . For

$$A = \frac{GM_p}{c_s^2 r_s}, \quad (6)$$

we require that $A < 1$ for the linear assumption to strictly hold. This estimates the density perturbation at approximately radius r_s , where r_s is the softening scale of the numerical potential (see [Section 3.1](#)). The A parameter effectively places a constraint on the physical scenarios that can be described by this prediction, since cases with very high mass perturbers, very small radii, or very large sound speeds, will violate the small A condition.

Any scenario can be completely described by two parameters: this A parameter, and the Mach number \mathcal{M} of the perturber. The predicted force, given by [Equations \(3\), \(4\) and \(5\)](#), can be used to test numerical results, and they were found to match the appropriate choice of A and r_{\min} ([Sánchez-Salcedo & Brandenburg 1999](#); [Kim & Kim 2009](#); [Bernal & Sánchez-Salcedo 2013](#)). As discussed in [Section 1](#), these works find the forces match when r_{\min} is chosen suitably. These studies all use Eulerian grid based codes for their numerical studies. No equivalent studies have been performed using

² See [Just & Kegel \(1990\)](#) for an alternative derivation

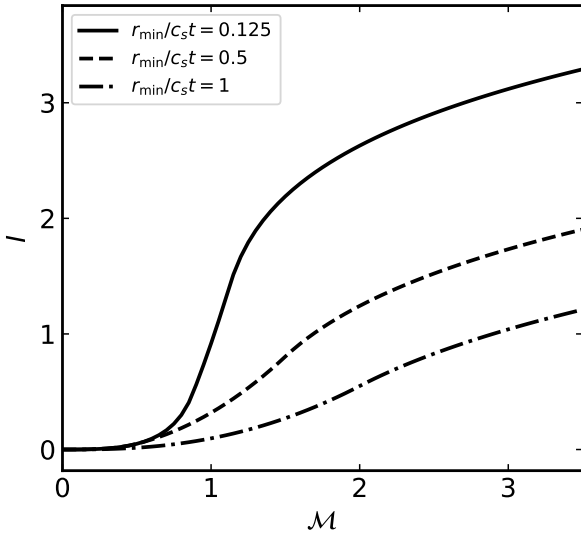


Figure 1. Value of integral I as a function of Mach number \mathcal{M} , for $r_{\min}/c_s t = 0.125, 0.5, 1$.

the moving-mesh-like approaches studied here. We therefore do not know how well these methods can capture DF and how they compare.

3 NUMERICAL METHOD

We run a set of idealised 3D gravohydrodynamic simulations of DF, using the state-of-the-art multiphysics codes Enzo (Bryan et al. 2014), Gizmo (Hopkins 2015), Gadget-4 (Springel et al. 2020) and Arepo (Springel 2010), comparing their output with both analytic predictions and previous numerical results. In this section, we describe our numerical approximation of the idealised case for DF, the key parameters used in the code setup, and the initial conditions of the simulations.

3.1 Setup

The numerical setup is designed to closely replicate the assumptions made in the derivation of the analytic solution. The initial conditions have a uniform density ρ_0 adiabatic gas, moving with a bulk velocity V_0 , in a 3D box with a fixed gravitational potential Φ from a massive perturber M_p . The bulk velocity has the Mach number $\mathcal{M} = V_0/c_s$. The gas does not experience self-gravity, and the boundaries of this box are periodic. In practice, this limits the time for which we can run the simulation, because we want to avoid the periodically extended wake influencing the numerical outcomes.

In the numerical case, it is necessary to use a perturber with a softened potential, to avoid the shot noise and other artifacts introduced by simulating a point mass perturbing a gas with finite mass and spatial resolution. This is equivalent to modelling a perturber with an extended mass distribution, which is most closely related to orbiting subhaloes or star clusters. It changes the shape of the wake in mostly minor ways, but, most notably in the supersonic case, it spreads the sharp Mach cone front over $\sim 2r_s$ (Furlanetto & Loeb 2002; Kim & Kim 2009). Because of this, we will focus on comparisons to the analytic solution for results in regions $> 2r_s$.

To facilitate comparisons to earlier numerical work we assume

that the massive perturber in our case has the form of a Plummer sphere (Plummer 1911), with potential

$$\Phi(r) = -\frac{GM_p}{(r^2 + r_s^2)^{\frac{1}{2}}}, \quad (7)$$

with mass M_p and softening r_s . This softening is analogous to the extent of the perturbing object. The simulation time is characterised by sound speed crossing time of this length $t_c = r_s/c_s$.

To reproduce the uniform initial density, we generate glass-like initial conditions (ICs) using WVTICs (Donnert et al. 2017; Arth et al. 2019). This combines a weighted Voronoi mesh with a particle shuffling method to reproduce arbitrary density distributions with a set of SPH particles. The ICs created with this method were found to be superior to simple initial grids and random particle placements, minimising both periodic oscillations in the net force on the perturber and initial variation in the local density distribution. For the Arepo comparison runs, we use these particle positions as the cell centres for the initial mesh.

The idealised set-up is effectively scale free, characterised by A in Equation (6) and the Mach number \mathcal{M} (Kim & Kim 2009). The A parameter sets the relationship between the perturber, from its mass and extent, and the medium, through the speed of sound. In this context, the extent is taken to be equivalent to the softening scale of the potential. It should be noted that the A parameter is defined by this softening scale, and the lower limit of the force integral r_{\min} plays no role in defining the setup. Instead, the lower limit functions as a numerical fitting parameter, as discussed above. While we initially take $r_{\min} = r_s$, this is not strictly required by the derivation. We choose to show forces calculated using $r_{\min} = r_s$ for simplicity unless otherwise stated. We present radial break downs of the net force that show what r_{\min} would produce a good fit in Section 4.3.

The relative motion is captured by the Mach number. We run setups for a range of Mach numbers, exploring the regime where collisional DF differs most from collisionless DF, for $0.7 < \mathcal{M} < 2.0$. We explore a range of resolutions, dictated by the number of particles. The Mach range is explored with $N = 256^3, 512^3, 1024^3$ particles, with the most samples at 512^3 . The different setups are summarised in Table 1. The size of the box L is varied in certain runs. Varying the particle number is used to effectively test the convergence of our results with resolution.

To test the numerically modelled gas under different conditions, it is necessary to explore the scale-free parameter space of A and Mach number. The setup is constrained by the periodic boundary conditions, setting an upper limit on how long the scenario can be run before the wake reaches the edge of the box, and so wraps around. This time is defined by the edge length of the box and the initial velocity of the gaseous background. A range of Mach numbers were probed, exploring the regime around the strongest gaseous signal at $\mathcal{M} = 1$. The majority of the boxes are run for $t = 15t_c$, with the larger boxes pushed to $t = 150t_c$. Each box was run until the wake reached close to the edge of the periodic box. If it were run longer, the edge of the over-density wake would rap around. Larger boxes allow for longer runs, but at the cost of reduced mass resolution, critical to recovering the small over-densities in the wake structure. Our setup reaches $t = 15t_c$ in the standard runs, and the largest boxes reach $t = 150t_c$, while still retaining acceptable mass resolution.

Table 1. Details of all the simulation runs. Solvers refer to either the `Gizmo`, `Gadget4`, `Arepo`, or `Enzo` codes, using either the MFM, PSPH, PPM or MUSCL schemes. N is the number of particles or cells, per edge length, t_{final} the end time of the simulation, in units of sound speed crossing time t_c of the softening length r_s , and L is the length of the edge of the cube box, relative to our standard box.

ID	Solver	N	\mathcal{M}	t_{final}	L
GM256M07	MFM	256	0.7	15	1
GM256M09	MFM	256	0.9	15	1
GM256M1	MFM	256	1.01	15	1
GM256M11	MFM	256	1.1	15	1
GM256M13	MFM	256	1.3	15	1
GM256M15	MFM	256	1.5	15	1
GM256M2	MFM	256	2	15	1
GM512M02	MFM	512	0.2	15	1
GM512M07	MFM	512	0.7	15	1
GM512M09	MFM	512	0.9	15	1
GM512M1	MFM	512	1.01	15	1
GM512M11	MFM	512	1.1	15	1
GM512M13	MFM	512	1.3	15	1
GM512M15	MFM	512	1.5	15	1
GM512M2	MFM	512	2	15	1
GM512M3	MFM	512	3	15	1
GM1024M07	MFM	1024	0.7	15	1
GM1024M09	MFM	1024	0.9	15	1
GM1024M1	MFM	1024	1.01	15	1
GM1024M11	MFM	1024	1.1	15	1
GM1024M13	MFM	1024	1.3	15	1
GM1024M15	MFM	1024	1.5	15	1
GM1024M2	MFM	1024	2	15	1
GM64M13	MFM	64	1.3	15	1
GM128M13	MFM	128	1.3	15	1
GM256M13	MFM	256	1.3	15	1
4P512M13	PSPH	512	1.3	15	1
GM512M13LM	MFM	512	1.3	15	1
GM1024M13L	MFM	1024	1.3	150	10
EP512M07	PPM	512	0.7	15	1
EP512M09	PPM	512	0.9	15	1
EP512M11	PPM	512	1.1	15	1
EP512M13	PPM	512	1.3	15	1
EP512M15	PPM	512	1.5	15	1
EP512M2	PPM	512	2.0	15	1
AM512M07	MUSCL	512	0.7	15	1
AM512M09	MUSCL	512	0.9	15	1
AM512M1	MUSCL	512	1.01	15	1
AM512M11	MUSCL	512	1.1	15	1
AM512M13	MUSCL	512	1.3	15	1
AM512M15	MUSCL	512	1.5	15	1
AM512M2	MUSCL	512	2.0	15	1
AM64M13	MUSCL	64	1.3	15	1
AM128M13	MUSCL	128	1.3	15	1
AM256M13	MUSCL	256	1.3	15	1

3.2 Codes

We primarily assess the gravitationally induced wake, and resulting effects, from the Lagrangian finite mass (MFM) (Hopkins 2015) solver in `Gizmo`. The MFM solver is a state-of-the-art hydrodynamics solver that discretises the volume using tracer particles and a chosen kernel function, and then solves the Riemann problem between neighbouring particles, utilising a high order gradient estimator. We use 32 neighbours, and the cubic kernel, for the kernel construction. To augment this assessment, we include comparison runs using the pressure-entropy smoothed particle hydrodynamics

(PSPH) solver in `Gadget4` (Springel et al. 2020), the piecewise-parabolic method (PPM) and the moving mesh MUSCL-Hancock implementation in `Arepo` (Springel 2010).

The PSPH solver is an extension to the standard SPH formulation (Gingold & Monaghan 1977). It estimates pressure gradients using entropy rather than density, reducing inaccuracies at fluid interfaces, and the required number of kernel particles. As before, we use 32 neighbours and the cubic kernel for the kernel construction. The idealised DF problem has not been investigated in detail using these modern Lagrangian solvers, so our understanding of their detailed behaviour in this context is currently limited and provides a further test for the numerical accuracy of these schemes.

We use the PPM solver in `Enzo` for comparison to the widely used grid based solver. This implementation is based on a modified version of the PPM method from Colella & Woodward (1984), adapted for cosmological settings. As the name implies, it solves the Eulerian fluid equations via piecewise parabolic reconstruction of the fluid state across a spatially discretised domain. We do not utilise the adaptive mesh refinement capabilities in `Enzo` in order to maintain the simplest resolution comparison.

Finally, we compare with results from the MUSCL-Hancock moving mesh scheme used in `Arepo`. This couples the slope-limited piece-wise reconstruction step with spatial decomposition that moves approximately with the fluid, aiming to combine the Lagrangian nature of particle codes with the precision of grid based approaches.

4 RESULTS

In this section, we compare the numerical results from simulations against the corresponding analytic predictions. We focus on the results with the MFM solver, unless otherwise stated. We first compare the structure of the numerical wake with the prediction from linear theory. In particular, we seek to identify the radius beyond which the two agree. To this end, we compare the net gravitational force acting on the perturber from the perturbed density, across Mach numbers and time.

4.1 Wake

We directly compare the numerical density distribution with the analytical prediction of the wake form, given by α in Equation (1). The numerical density is averaged by dividing the particles into cylindrical bins (s, R) . This is then normalised to the dimensionless over-density $\alpha = (\rho - \rho_0)/\rho_0$. Here s is the distance from the perturber along the direction of travel, and R is the cylindrical radius away from this axis. In Figure 2, we show the structure of the numerical over-density, with contours showing the analytic prediction (white dashed lines), for four Mach numbers, $\mathcal{M} = 0.7, 0.9, 1.3, 2$. The residual (here the difference between numerical and analytic results) shows us that the main difference is in the front of the Mach cone structure. The sharpness of the density peak in the cone has been softened, with the density smeared into a wider profile. The peak in the cone over-density is too small and extends too far forward. The smearing of the profile is on a scale larger than the spatial resolution of the simulation l , with the profile spread over approximately $20l$. These features are clearly seen in Figure 3, where we show the over-density α on a line of constant $R = 2r_s$, for $A = 0.1$. Each Mach number is shown in a different panel, from top to bottom $\mathcal{M} = 1.1, 1.3, 1.5$, with the solid line showing the analytic solution, and the dashed line showing the numerical result. In Figure 3 we

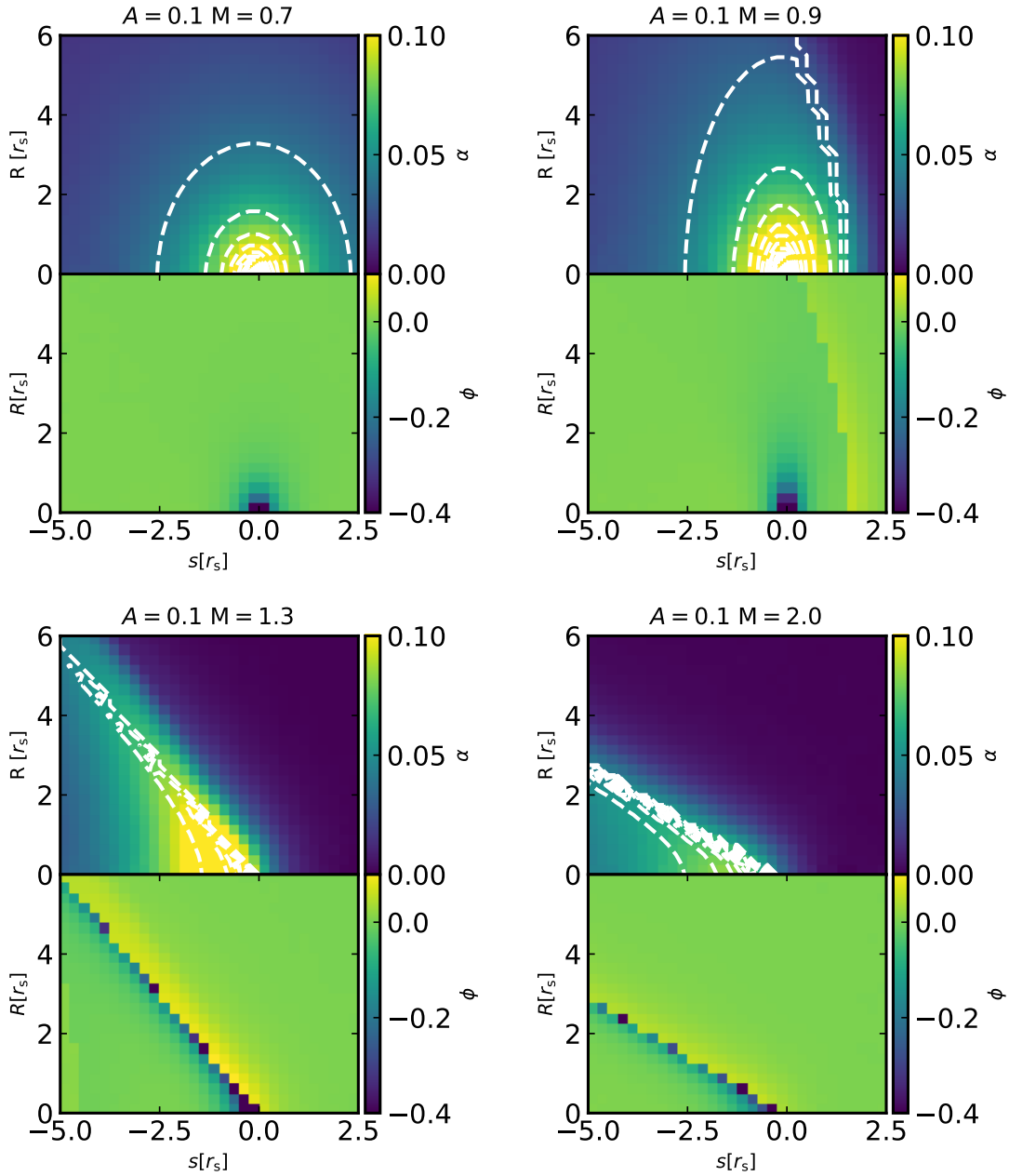


Figure 2. Zoomed view of over-density across $\mathcal{M} = 0.7, 0.9, 1.3, 2.0$, at $t = 15t_c$, using $N = 1024^3$ (runs GM512M07, GM512M09, GM512M13, GM512M2). The upper part of each panel shows the numerical over-density α_{num} in colour and the analytic prediction for the over-density α_{ana} as white dashed contours. We see the development of a bow shock like structure ahead of the perturber. The difference between these distributions $\phi = \alpha_{\text{num}} - \alpha_{\text{ana}}$ is shown in the lower part of each panel.

also compare the Gizmo MFM results to the MUSCL scheme in *Arepo*, and to the PPM scheme in *Enzo*, which all match each other very closely.

The spread in the numerical result is caused by the extended nature of the perturber. The analytic solution assumes a point mass. If that mass is instead spread across some spatial distribution, the resultant wake will be approximately a convolution of the point mass solution with the mass distribution. Our results are consistent with previous work, which finds that extended perturbers with softening scale r_s produce spreading from the cone front of $\sim 2r_s$ (Furlanetto & Loeb 2002). The structure is generally well matched at large radii

from the perturber, where the over-density is very small. While the exact structure of the wake is important for recovering the perturbation of the background medium, it is the resultant retarding force on the perturber that is often studied.

4.2 Force

We examine how the moving mesh simulations of the Plummer perturber compare with the analytic predictions for a point mass from Ostriker (1999). Included in this is how the comparison varies with numerical resolution. The wake does not match at small radii,

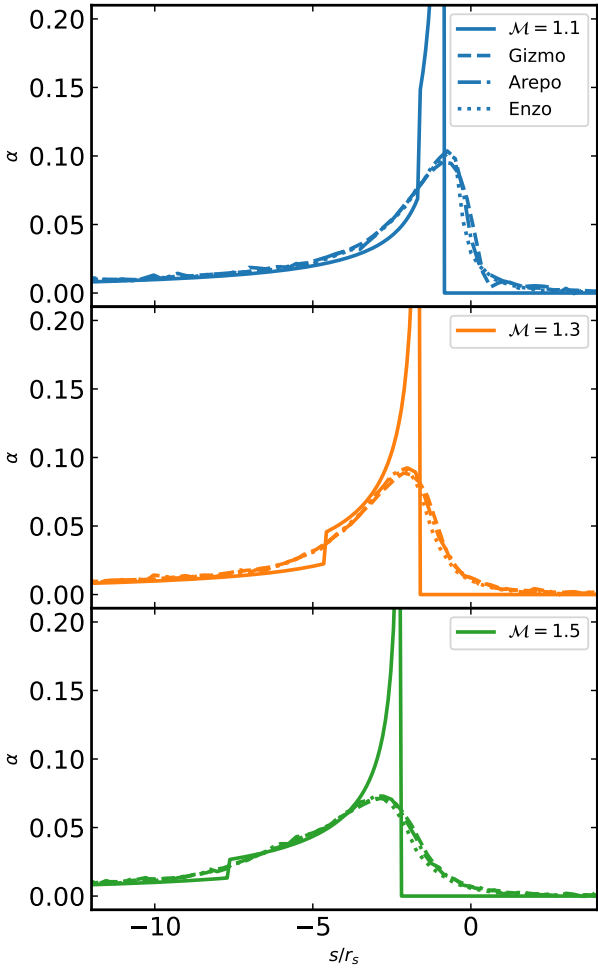


Figure 3. Profile of over-density α along a line of constant $R = 2r_s$, at $t = 15t_c$, with $\mathcal{M} = 1.1$ (top), $\mathcal{M} = 1.3$ (middle), and $\mathcal{M} = 1.5$ (bottom). The profiles are from the same results as those shown in the left column of Figure 2. Solid lines show the analytic solution, dashed lines show the Gizmo results, dash-dot lines show Arepo, and dotted lines Enzo.

as discussed above, but we study the radius beyond which the force is the same. As mentioned in the introduction, the [Ostriker \(1999\)](#) solution is applied directly as a subgrid model in simulations, and as a drag term in analytic and semi-analytic works. We show how these solvers predict deviations from the analytic point-mass solution for an extended perturber, in this case a Plummer sphere, and compare this to previous numerical results. This is the significance of the exploration of force and r_{\min} that follows below.

The prediction from linear theory for the net gravitational force on the perturber is given by Equation (3). In the subsonic case, this solution to the integral holds for $r_{\min} < (c_s - V_0)t$, which requires the wake to be larger than the effective size of the perturber. For supersonic cases, the solution is found by assuming $r_{\min} < (V_0 - c_s)t$, which means that the lower limit of the integral is within the Mach cone. A numerical integration of the analytic over-density α is used at times when these conditions were not satisfied. For example, this would happen if the cone is entirely inside r_{\min} , but not the spherical part. This allows us to produce an accurate force for the analytic wake solution, no matter the limits of the integration. It is achieved by explicitly breaking the wake into zones, with cone and sphere sections, and then integrating the sections separately

based on where r_{\min} falls. The equivalent force from the simulation output is calculated by direct force summation. The Newtonian gravitational force is calculated between each particle of mass M_{part} and the massive perturber M_p . All particles within $r < r_{\min}$ of the perturber are excluded from the calculation.

The force is dependent on the Mach number and time. In Figure 4, we show the variation in the numerical and analytic forces with Mach number for three sets of runs at $t = 15t_c$. The three cases are for different resolutions, defined by the number of particles used. We again include results produced with Arepo, as a check against another widely used code. Gizmo results are shown as circles, Arepo as squares, with the colour showing the resolution (see figure for specifics). The bottom panel shows the absolute value of the residual $|\phi| = |F_{\text{num}} - F_{\text{ana}}|/F_{\text{ana}}$. The subsonic setups show reasonable agreement at $\mathcal{M} = 0.7$, with some divergence at $\mathcal{M} = 0.9$. The residual is significantly higher at $\mathcal{M} = 0.2$, due to a very small absolute value of the force. DF in this regime is not consequential to actual physical scenarios.

We start by exploring how the numerical Plummer and analytic point mass forces compare when integrating out from the natural inner limit of $r_{\min} = r_s$. The supersonic cases show the most marked differences. The forces are 10 – 25% lower than expected. The difference is most extreme in the supersonic regime close to $\mathcal{M} = 1$. At larger Mach numbers $\mathcal{M} \geq 2$, the numerical results show significantly less difference and therefore match better with the point mass solution. The analytic force is also smaller, in this regime, so perturbing objects will experience less drag. We therefore focus our analysis and discussion to $0.7 < \mathcal{M} < 2$, where the absolute and proportional differences are most pronounced, and most consequential. This is also the most likely range of Mach numbers for perturbers, such as galaxies and subhaloes orbiting within a host halo. These differences are significant because they show that the solvers used here predict that an extended perturber (in this case a Plummer perturber) will produce less drag force than if one assumes the point-mass [Ostriker \(1999\)](#) solution. The latter is commonly used as a sub-grid model.

The net drag forces show only small variation with resolution. The green dots in Figure 4 show the runs using $N = 256^3$, while the orange dots show $N = 512^3$, and the blue dots $N = 1024^3$. The orange and blue points match within 5%. The green, being the lowest resolution, are more scattered from the underlying pattern, but are still broadly consistent. This demonstrates that we have converged on consistent numerical results, at the 5% level, in terms of both mass and spatial resolution. The Arepo results fit closely with those from Gizmo. Therefore, the results have converged when we increase the mass resolution and spatial resolution. The wake is still smeared out in comparison to the analytic solution. This must come either from the extended nature of the perturber, or the solver. As the results from the different solvers agree closely, we conclude the difference is purely created by the extended perturber.

As presented above, we chose first to calculate results for $r_{\min} = r_s$, as shown in Figure 4. It is clear that parts of this numerical wake differ from the point-mass prediction for the reasons discussed above. However, we are still interested in where the force from an extended perturber is consistent with the equivalent force from a point mass. As one moves away from an extended perturber, the gravitational potential of the perturber appears increasingly like a point mass. To this end we explore at what r_{\min} the two become broadly consistent. We find that the force from $r_{\min} = 4r_s$ is approximately consistent with the analytic prediction. When $r_{\min} = 4r_s$, the numerical force results are within 5% of the expected value. The forces produced when this fit is used are shown in Figure 5.

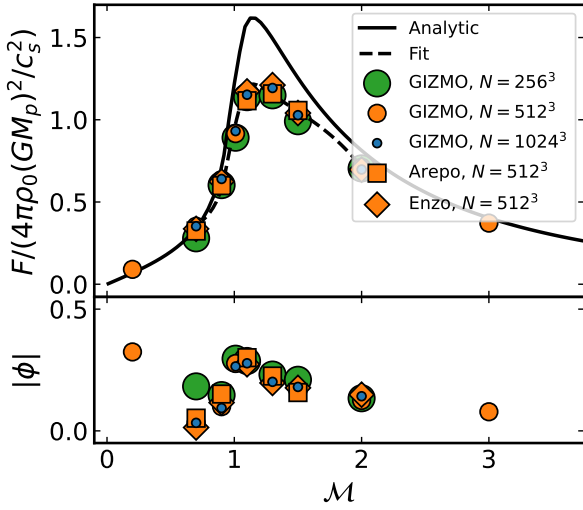


Figure 4. *Upper Panel:* Dimensionless force from numerically induced wakes across a range of Mach numbers, at $t = 15t_c$. We show results from GIZMO (circles), Arepo (squares), Enzo (diamonds), and the corresponding analytic prediction (black line). The dashed line shows the fit produced when we apply a conversion factor to the point mass solution (see Section 4.4). We show runs using $N = 256^3$ (green), 512^3 (orange), and 1024^3 (blue) particles/cells. The force is calculated using $r_{\min} = r_s$. It diverges significantly for supersonic cases close to $\mathcal{M} = 1$. The 512^3 and 1024^3 agree well, with differences within the 5% level, while the 256^3 broadly agree, though do show increased scatter. *Lower Panel:* Absolute residual between the numerical and analytic results $|\phi| = |F_{\text{num}} - F_{\text{ana}}|/F_{\text{ana}}$.

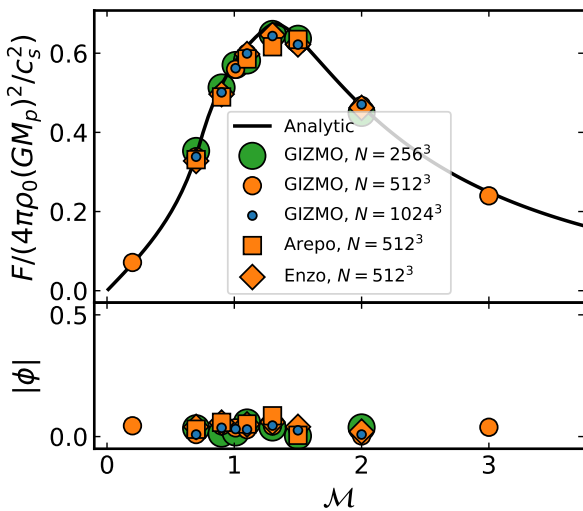


Figure 5. Same as Figure 4, but using $r_{\min} = 4r_s$. All cases now match within 5%, in both subsonic and supersonic regimes.

We check how the force contribution changes with r_{\min} to demonstrate the validity of this fit. Figure 6 shows a breakdown of the absolute residual between the numerical and analytic forces, contributed from spherical shells of width $\sim r_s$ centred at radius \bar{r} , for different Mach numbers. We show $\mathcal{M} = 0.7$ (blue), 0.9 (orange), 1.01 (green), 1.1 (red), 1.3 (purple), 1.5 (brown), 2 (pink). As before, the largest variation is found close to $\mathcal{M} = 1$, with the bulk of the divergence coming within $r_{\min} = 2r_s$. We see that the forces match within 10% per bin for all cases when $r_{\min} \geq 4r_s$, except

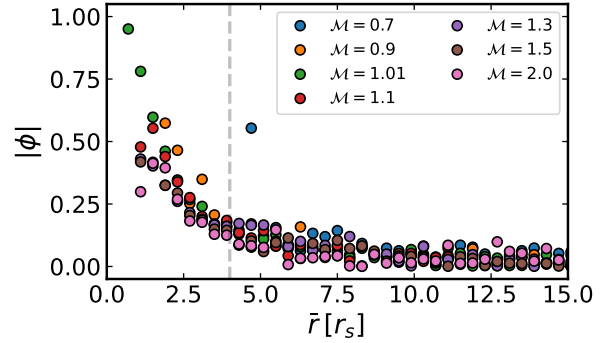


Figure 6. Absolute residual of force contributed from spherical shells of width r_s , centred at \bar{r} , using $N = 1024^3$ runs. We show $\mathcal{M} = 0.7$ (blue), 0.9 (orange), 1.01 (green), 1.1 (red), 1.3 (purple), 1.5 (brown), 2 (pink). Dashed grey line marks position of the fit at $r_{\min} = 4r_s$. Force in all bins beyond this point matches to within 10%, at all Mach numbers except $\mathcal{M} = 0.7$. Here the values are very small, so numerical variation is high.

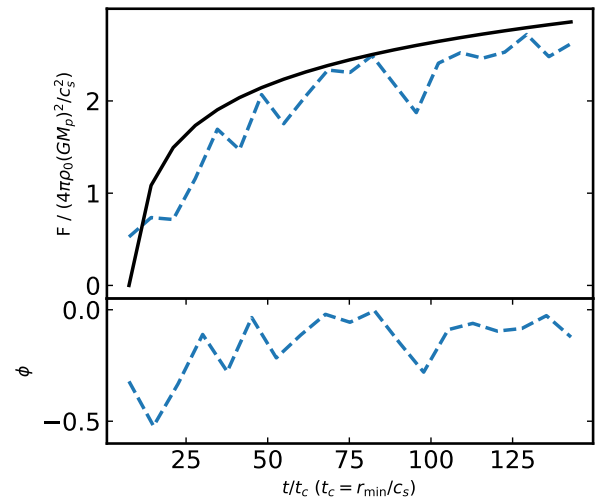


Figure 7. *Upper Panel:* Time evolution of the dimensionless force in the larger $L=100\text{kpc}$ box. The force does not converge to the analytic solution in this longer time. *Lower Panel:* Residual between analytic and numerical results $\phi = (F_{\text{num}} - F_{\text{ana}})/F_{\text{ana}}$. Lower integral limit is $r_{\min} = r_s$.

at $\mathcal{M} = 0.7$, where the force contributions are all so small that numerical noise creates large variations. Although the results per bin differ at the 10% level, the force of the whole wake is within 5% across our Mach number range. These differences are consistent with the spreading of the sharp cone front, as the impact of this on the gravitational force experienced by the perturber would diminish with distance. Higher Mach cases have more extended cones. The difference is most pronounced very close to the perturber, where the spreading would push some mass in front of the perturber, cancelling some of the drag force. Further out, the spread would all be behind the perturber.

Previous numerical studies, which also use Plummer spheres, have produced their own r_{\min} fits (Sánchez-Salcedo & Brandenburg 1999; Kim & Kim 2009). We will compare our results to these fits, in detail, in Subsection 4.4.

4.3 Long Term Evolution

So far we have shown results $15t_c$ after the perturber is turned on. Previous works (Sánchez-Salcedo & Brandenburg 1999; Kim & Kim 2009) report results at many hundreds of crossing times. At these times the wake has reached scales hundreds of times the gravitational softening scale of the perturber. The results of the larger box are shown in Figure 7, using GM1024M13L, which extends the run time to $150t_c$. All forces shown here are calculated using $r_{\min} = r_s$. The intrinsic variation in the force is larger for these larger boxes, where $M_{\text{part}}/M_p = 8 \times 10^{-7}$ (see Appendix A). In summary of this variation, the discretisation of the gas by mass leads to some fluctuation in the net force on the perturber. This fluctuation is greater when the mass ratio of the particle to perturber is large, since a single particle can exert a greater force on the perturber. This effectively places some limits on the setups that can be feasibly run, since very large random variation will prevent meaningful results from being extracted from the simulation output. However, we can still conclude from this longer run that the difference in force from the extended perturber continues to large times.

Testing the convergence of results based on resolution, via the number of particles, produces the same evolution whether we use $N = 64^3$, 128^3 , 256^3 , 512^3 or 1024^3 particles, in effect increasing the spatial resolution from $0.8r_s$ to $0.05r_s$. The bulk velocity and sound speed of these runs are identical, with only the particle mass changing. This maintains the same background density. This force evolution is shown in Figure 8. The random variation discussed above is effectively dependent on the ratio of the particle mass to the perturber mass. While the lower resolution runs show much greater scatter over time, they are broadly consistent with the higher resolution cases. The exact form of the wake also converges, showing the same structure at $N = 256^3$ as at higher resolution. This corresponds to convergence at a spatial resolution of $0.2r_s$. This is roughly equivalent to 5 cells per gravitational softening scale in a grid based code. At resolutions below this, the resolution is too low to practically assess the shape of the detailed structure of the wake.

On top of the tests we present above, we also run verification tests that vary the exact conditions used in the numerical runs, such as perturber mass and initial background gas conditions. These should not impact the results found here, as the problem is effectively scale-free to these variables, and indeed this is what we find. These changes have no impact on the wake structure or the resultant drag force.

The results presented in Sections 4.2 to 4.3 show that the force fits the force predicted for a point masses, when $r_{\min} = 4r_s$. There is no obvious change in the force trend, even at large times. Our runs have converged, within 5%, at the high resolution end, and show good agreement at lower resolutions.

4.4 Minimum Radius Fit

As discussed in Section 4.2, we have found the radius beyond which our numerical results produce a drag force that matches the equivalent analytic point-mass force. We aim to demonstrate how the forces from different numerical studies of extended perturbers produce different predictions for the distance beyond which the force matches that from a point-mass. We now compare the resultant force produced by our numerical results when we use the various fits described in previous works. We compare to KK09 and BS13, which are $r_{\min} = 0.35M^{0.6}r_s$ and $r_{\min} = 2.25r_s$ respectively. The $r_{\min} = 2.25r_s$ fit is also used by Sánchez-Salcedo & Brandenburg (1999).

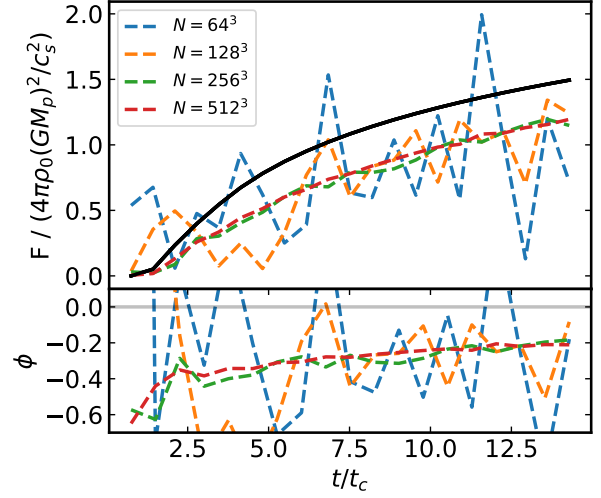


Figure 8. *Upper panel:* Evolution of the dimensionless force for different particle numbers, showing $N = 64^3$ (blue), $N = 128^3$ (orange), $N = 256^3$ (green), $N = 512^3$ (red). The evolution is essentially identical for all resolutions, but with significantly increased random variation for $N = 64^3$ and $N = 128^3$. All forces are calculated using $r_{\min} = r_s$. *Lower panel:* Residual between numerical and analytic wakes $\phi = (F_{\text{num}} - F_{\text{ana}})/F_{\text{ana}}$.

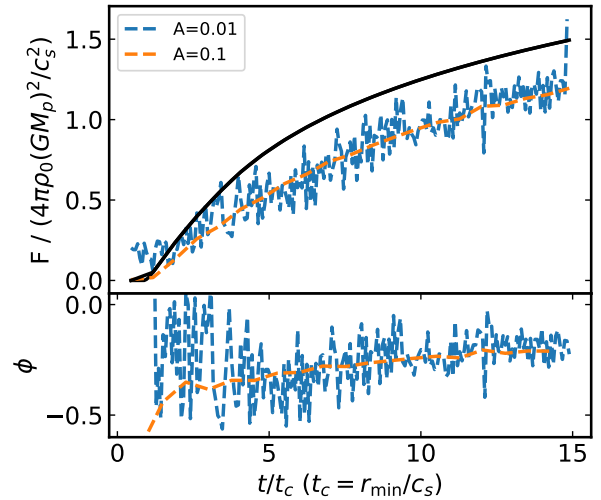


Figure 9. *Upper panel:* Evolution of the dimensionless force for $A = 0.01$ (blue) and $A = 0.1$ (orange), using runs GM512M13LM and GM512M13 respectively. The evolution is essentially identical for all resolutions, but with significantly increased random variation for $N = 64^3$ and $N = 128^3$. All forces are calculated using $r_{\min} = r_s$. *Lower panel:* Residual between numerical and analytic wakes $\phi = (F_{\text{num}} - F_{\text{ana}})/F_{\text{ana}}$.

The previous studies use runs at $A = 0.01$. While most of our runs use $A = 0.1$, we have run a comparison case using $A = 0.01$ GM512M13LM, achieved by reducing the perturber mass by an order of magnitude, and which does not show a different evolution. This case shows a much greater innate variance due to the lower ratio of element mass to perturber mass (see Appendix A for a detailed explanation). The overall trend in force from this case, however, is the same as the $A = 0.1$ case, but with increased variance. This is shown in Figure 9, with $A = 0.01$ in blue and the standard $A = 0.1$ in orange.

In Figure 10, we show the fractional residual between the

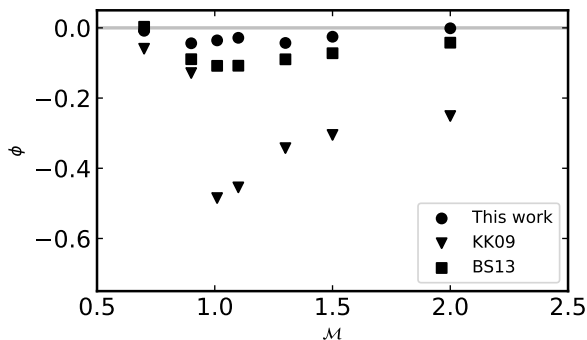


Figure 10. Residual $\phi = (F_{\text{num}} - F_{\text{ana}})/F_{\text{ana}}$, between the numerical and the expected analytic forces, using fits found in this work (circles), KK09 (triangles), and BS13 (squares).

extended and point mass perturber forces, using the different fits for r_{min} . The circles show the results using the fits from this work, the triangles use the fit from KK09 and the squares the fit from BS13. This figure shows that the fits found in previous works do not produce accurate forces from our numerical wakes, for $0.7 < \mathcal{M} < 2$. With $\mathcal{M} \leq 0.7$, all fits produce forces that match within 5% of the prediction. At the other end of the tested range, where $\mathcal{M} \geq 2$, all but the KK09 fit produce close matches. This is consistent with our previous results, as both fits produce smaller minimum radii. It confirms that the extended nature of the perturber creates a difference in forces that is most pronounced in the range $0.7 < \mathcal{M} < 2$.

The fit we identify here is based on a systematic search of the minimum radius of the force integration. The radius at which the fractional residual drops to $\phi \leq 0.01$ is shown in Figure 11. The exact radius at which this happens is not constant with Mach number, so the final fit is an approximation, and only holds for the stated Mach range of $0.7 < \mathcal{M} < 2.0$. There is scatter of order r_s about the mean values shown here, so the final fit is an approximation at this level.

The minimum radii found from previous works are also shown. Some of the Mach number runs do not achieve a match within 1%, so these are not included in the plot. The key result here is the difference in force that we predict from an extended perturber. Note that we are comparing our full 3D results with results from 2D simulations. These works implicitly assume that their results are rotationally symmetric, as does the analytic solution. In essence, they extrapolate their results from 2D to 3D. Our results effectively average over these fluctuations, but they are still present in our final results. However, on inspection, we find that there is little fluctuation across different slices through the full 3D wake.

We now directly compare the force produced by the r_{min} values found in the different numerical studies, normalised by the point mass analytic prediction. Figure 12 shows this normalised force produced by one of our numerical wakes when we use the different fits for minimum radius. The black dashed line shows the force produced by the numerical results, while the coloured lines correspond to the analytic force, with the colours emphasising the radii beyond which the different extended perturber studies match the point mass solution. As has been shown before, our fit for r_{min} produces a force that matches the point mass prediction to within 5%. The extended perturber wake found here creates a retarding force that is 33% less than that of the Ostriker linear prediction when we use the KK09 result, and 10% less when using BS13. Comparing between them,

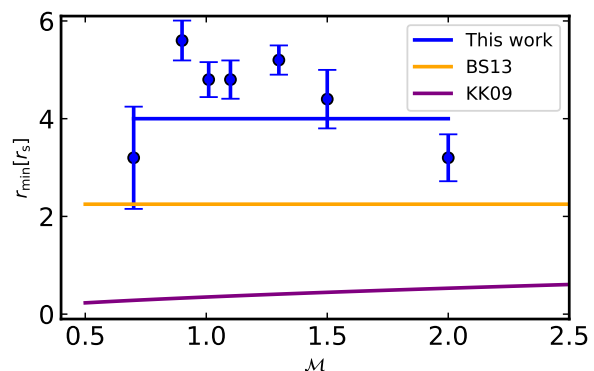


Figure 11. Minimum radius beyond which the force integration of the numerical wake produces a retarding force that is within 1% of the predicted force. Our results (blue dots) are shown, with the corresponding fit shown as the blue line. Error bars are found by taking the standard deviation of the r_{min} found for the last five snapshots of each run.

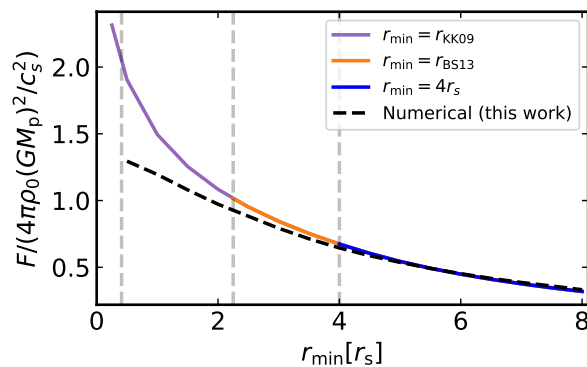


Figure 12. Drag force to the analytic prediction for a point mass, at $\mathcal{M} = 1.3$, using MFM and $N = 512^3$ (run GM512M13), for different minimum radii r_{min} . The forces produced by the numerical wake for each r_{min} fit are shown by the grey dashed vertical lines. In order these are KK09, BS13, and this work. The coloured lines show the force from the Ostriker point mass solution at the same minimum radius. These lines are limited to the radii where the different results match the point mass solution.

the BS13 result produces approximately 75% of the force from the KK09 fit, while this work produces about 55% when compared to KK09. The possible explanations for this will be discussed in the next section. It should be noted that some aspects of the exact process of producing these fits are not described in detail, so there is a chance we are not comparing exactly like-for-like when contrasting the different fits.

Ostriker considers r_{min} to be the effective extent of the perturber, since it is the edge of the region in which the linear solution is valid. In the context of the extended perturber studies this definition of r_{min} is dependent on the gravitational softening scale of the extended object, which is a measure of this extent. As mentioned in the introduction, the Ostriker solution is sometimes included as a sub-grid model to apply unresolved gaseous dynamical friction. Our results, and those of previous works, find that an extended perturber only matches the point mass case beyond certain radii. We can apply a factor to convert the point-mass analytic solution to fit our numerical results. In this case we use a third-order polynomial

and find the function

$$C(\mathcal{M}) = -1.03\mathcal{M}^3 + 4.61\mathcal{M}^2 - 6.48\mathcal{M} + 3.68. \quad (8)$$

The Ostriker solution is simply multiplied by this function to give a good approximation of the trend found in our numerical results. This is shown as the dashed line in Figure 4. The fit is for $0.7 < \mathcal{M} < 2.0$. This would convert the analytic solution to match our numerical results. Since the previous numerical studies find different r_{\min} fits, they would also have different conversion functions.

5 DISCUSSION

This work represents the first numerical study of dynamical friction using this class of meshless hydro solver, in this highly idealised context. We find a fit of $r_{\min} = 4r_s$ beyond which the wake produces the retarding force predicted by linear theory for a point-mass perturber. This is somewhat different from previous numerical studies, but is approximately consistent. Below we discuss implications for cosmological simulations, and the usefulness of this setup as a standard test for hydrodynamics modelling in astrophysics.

5.1 Nature of Solver and Resolution Comparisons

The Lagrangian nature of some of the methods used here means that spatial resolution comparisons with previous work on Eulerian grids are not simple. The kernel lengths in a typical run are of order $0.1r_s$, compared to 1 cell per r_s (Sánchez-Salcedo & Brandenburg 1999), or 5 cells per r_s and 6 cells per r_s , in KK09 and BS13 respectively. In our results, we see convergence in the evolution of the wake from at least 5 cells per r_s . Similarly, using the Gadget4, Arepo or Enzo solvers does not change our findings, so the differences in wake and force evolution are not unique to the Gizmo MFM solver.

Another crucial aspect of numerical schemes is the integration time-step. We tested if the standard time-step could be the source of the mismatch by reducing the integration time step by an order of magnitude. This change has no effect on the evolution of the wake. Similarly, we varied the number of neighbours used in the PSPH runs, again with no change in the results. Finally exact physical conditions were varied, such as background temperature, perturber mass etc. all while maintaining the same Mach number and A number. Again this did not alter the resultant normalised force or wake evolution.

It is not obvious why we find so different values for the regime in which the extended perturber matches the linear point-mass solution. KK09 speculate that their difference with other studies could be caused by the use of different equations of state. BS13 however test this and rule out the possibility. Neither work gives the specific method to find the fit for r_{\min} , so it is possible that some of the differences are caused by different fitting methodology/tolerance. Similarly, the exact process of calculating the force from the numerical wake could differ. We may, therefore, not be making an exactly like-for-like comparison, but we are doing so as best we are able. The previous works are both run in two dimensions, while our work is in three dimensions. However, there is no significant variation in slices at different angles, and no difference is expected under these highly idealised circumstances. The difference in dimension should therefore not create the difference in r_{\min} fits. Finally we perform our comparisons at an earlier time (in terms of crossing times), than the previous works. This is caused by the setup of the particle-based codes. Our long-time study suggests that we find approximately the same force level, relative to the point mass prediction, as late as

$t = 150t_c$. The variations in the results from this run are higher, as it had to be run at lower mass resolution. There is some scope there, if we could perform high-resolution long-term runs, to test if we come into agreement with BS13 at later times. However, the differences with KK09 are likely too large to be consistent even with the late-time results.

5.2 Implications for Cosmological Simulations

We have shown that the force only matches the linear theory beyond our r_{\min} fit, across many crossing times, using both MFM and PSPH type solvers. Here we discuss how the idealised setup used here could map onto the dark-matter substructure in cosmological simulations, and if we can draw any conclusions about the capturing of the DF they should experience.

The typical conditions in which we find subhaloes in cosmological simulations can be mapped onto the idealised point-mass setup by estimating their approximate Mach number and A parameters. We have taken the simulation results from the IllustrisTNG-300 public data (Nelson et al. 2019), using the halo and subhalo catalogues at $z = 0$. We selected all host haloes in the mass range $M_p = 10^{11}M_\odot$ to $10^{15}M_\odot$. The distribution of masses and sound speeds for all subhaloes are shown in Figure 13. The top plot shows the conditional probability of a sound speed, given a subhalo mass. The sound speed depends only on the mass of the host (see Appendix B), which leads to the bands at the end of high sound speed/host mass, where there are the fewest samples. We effectively see the negative slope in the power law distribution of halo/subhalo masses, as there are many more subhaloes associated with low mass haloes (low sound speeds), even though the most massive haloes individually contain far more subhaloes than any given lower mass halo. The middle plot shows the mean Mach number for each pixel. The distribution is fairly uniform across both mass and sound speed. The mean Mach number is around $\mathcal{M} = 1 - 2$. This is also shown in the top panel of Figure 14 with the conditional probability of a Mach number, given a subhalo mass. The bottom plot of Figure 13 shows the mean A parameter for each pixel. The distribution at the high subhalo mass end is dominated by small numbers of very high A parameter values in each cell. The overall distribution of A parameters are shown in the middle panel of Figure 14. The distribution has been truncated to $A = 10$, but continues to values in the thousands. We show the conditional probability of finding an A number, given a subhalo mass. The subhaloes below $M_p = 10^{10}M_\odot$ exist well within the linear regime ($A \ll 1$). Those between $M_p = 10^{10}M_\odot$ and $10^{11}M_\odot$ show a wider range of A , numbers, but still mainly reside in the linear or quasi-linear regime ($A \leq 1$). Above this mass, the distribution spreads significantly, with a range of A numbers, a significant fraction in the non-linear regime ($A > 1$).

The IllustrisTNG-300 subhaloes show that a large fraction of subhaloes in a typical state-of-the-art cosmological simulation exist within the linear DF regime, with $A < 1$, and with Mach numbers in the range $\mathcal{M} = 1 - 2$. This is the regime in which we have performed our numerical study, and the one in which gaseous DF is most impactful. The bottom panel of Figure 14 show the distribution of sound speed crossing times for the radial extents of these subhaloes. We see that these values are of the order $10 - 100$ Myrs.

A number of factors make DF in a system with more complete physical processes diverge from the analytic solution. The gas will obviously experience self gravity, leading to the further growth of the overdense wake. Radiative cooling mechanisms move the gas away from the adiabatic scenario considered in the analytic solu-

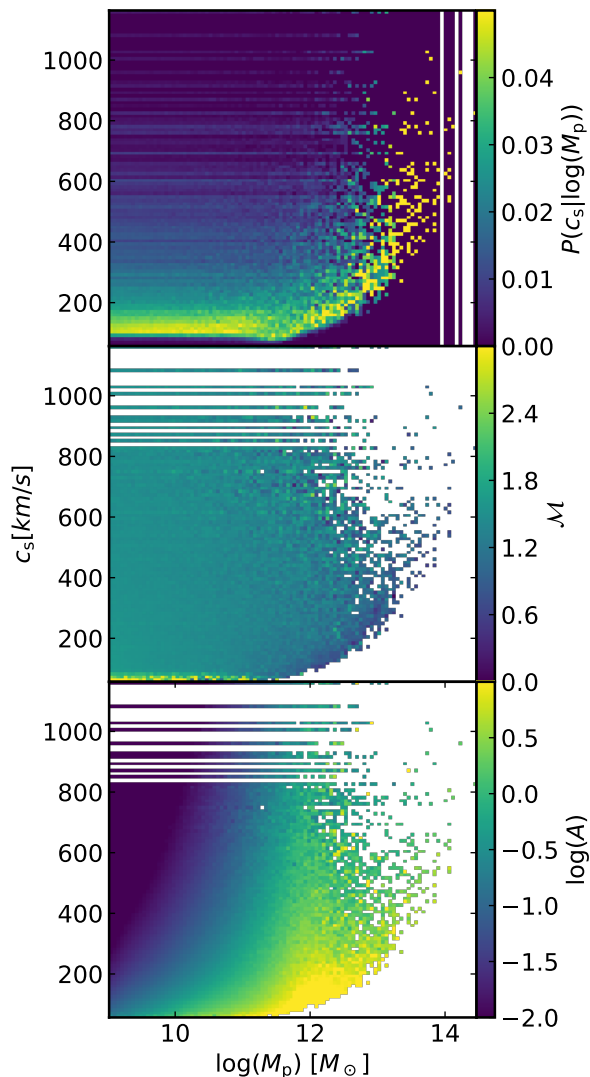


Figure 13. subhaloes from the IllustrisTNG-300 simulation box at $z = 0$. Sound speeds are calculated from the virial temperature of the host halo, dependent on the virial mass M_{200} . All panels show the subhaloes with masses between $M_p = 1 \times 10^{11} M_\odot$ and $1 \times 10^{15} M_\odot$, binned into subhalo mass - sound speed pixels. *Top panel:* The colour in this panel indicates the conditional probability of finding a sound speed, given a certain subhalo mass. *Middle panel:* Average Mach number of the subhaloes in each (M_p, c_s) pixel. The subhalo velocity is taken as the peculiar velocity of the subhalo, relative to the velocity of the host halo. *Bottom panel:* Average A value in each (M_p, c_s) pixel. The softening scale equivalent radius is taken to be the radius of the max velocity, based on the density profile of the subhalo.

tion. Feedback mechanisms from star formation, such as supernova driven winds, will also have complex effects. These will all be present in the full cosmological context of a cosmological simulations. The effect of these processes will be to significantly change the structure of the wake in complex ways.

While we have assumed, in our idealised setup, that the background medium has a uniform density, the simulated medium through which the subhaloes move will be far from uniform. The CGM is highly variable, made up of gas with a huge range of sound speeds. The wake will not build up smoothly as shown in the idealised scenario, where it can grow for an unlimited time through

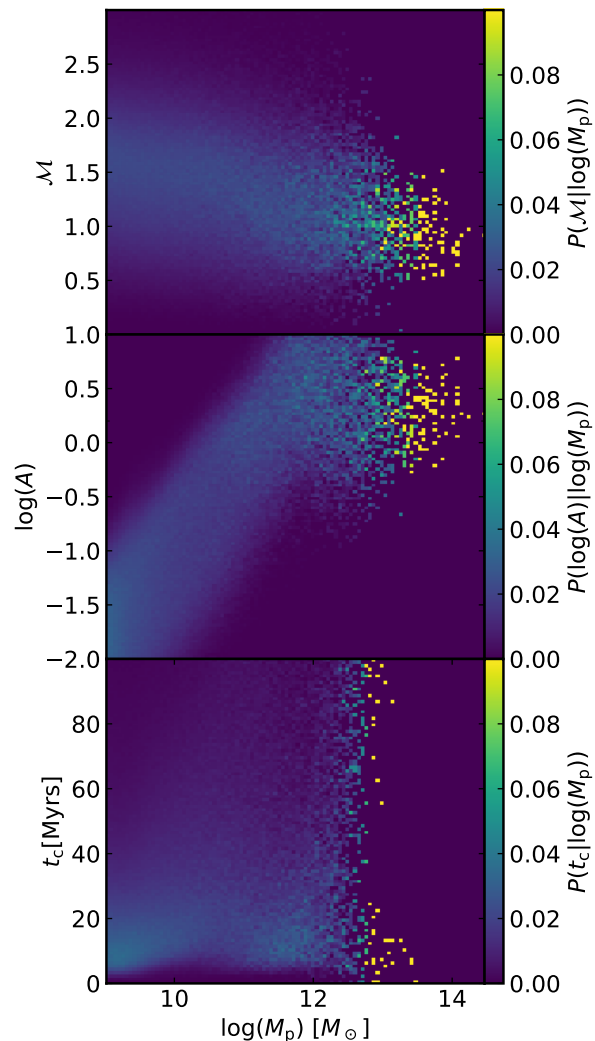


Figure 14. *Top panel:* Conditional probability of finding a Mach number, given a subhalo mass. The majority of subhaloes have mach numbers in the $\mathcal{M} = 1 - 2$ range. *Middle panel:* Conditional probability of finding an A number, given a subhalo mass. subhaloes with masses below $10^{10} M_\odot$ all exist well within the linear regime ($A \ll 1$). Above this mass, a significant fraction in each mass bin are either in the transition regime, or into the non-linear regime. *Bottom panel:* Conditional probability of finding a crossing time, given a subhalo mass. This crossing time is defined as the sound speed crossing time of the radial extent of the subhalo. For subhaloes of mass $10^9 M_\odot$ to $10^{12} M_\odot$ there is large spread of crossing times, with broad peak at $t_c = 10 - 30$ Myrs.

an infinite uniform background medium. Instead, at any given time, the wake will be built from the medium that the perturber (subhalo) is moving through at that time.

All of these processes aside, one major aspect of the environments around these substructures is how many particles make up the wake, however it ends up structured. Our study pushes down to $N = 64^3$ particles, but this is likely still larger than the numbers of particles used to resolve the substructure environs. We found that the force from the wake at this resolution shows large random variations, created by numerical noise, but that it does vary around the same value as that found at much higher resolution. It is therefore plausible that DF over longer enough time scales, is being captured correctly in these simulations. This is all the more important be-

cause many of these subhaloes exist in the regime where gaseous DF has its strongest effect. It is also important to remember that we have only considered the linear component of DF, and that the non-linear parts must also be considered in the capturing of DF if we are to model the process accurately.

5.3 Gaseous DF as a Standard Grav-Hydro Test

As we have seen in the preceding sections, the idealised gaseous dynamical friction problem presents a tough challenge for modern gravo-hydrodynamical solvers. It combines both gravitational forces and fluid dynamics, and includes complex flows which will not be aligned with any underlying structured mesh. The presence of the Mach cone, with its sharp density profile, one which is not aligned directly with, or orthogonal to, the bulk flow is a particular challenge. These factors make this setup an ideal candidate for a standard numerical test case for multi-physics astronomical codes. The problem has a well-defined analytic prediction for both the structure of the overdense wake, and the force produced by that wake. This allows for direct assessment of the accuracy of the numerical results, something that is relatively rare for tests that include complex, multidimensional fluid flows, one which includes the effects of both fluid and gravitational forces. The process of DF is also present across a range of important astrophysical problems and is a critical part of many of them, so understanding the abilities of our numerical methods in this area is important for our wider understanding of the underlying physics of these systems.

An additional strength of this problem, as a standardised test, is its scale-free nature. Any setup of the problem can be exactly defined by only two parameters, the A value, which effectively defines the linearity of the problem, and the Mach number \mathcal{M} . Any combination of sound speed, perturber mass, and potential softening can be compared using these scale-free parameters. The only limit in comparing to the analytic solution is that of linearity. In other words, the analytic solution assumes the wake is linear at all positions used in the comparison, such that the comparison is best made at $A < 1$. It is therefore extremely easy to directly compare multiple sets of numerical results to the analytic prediction, and to one another. For instance, reproducing plots such as that shown in Figure 4, compares results across A and \mathcal{M} to the analytic solution.

We propose this setup of a massive perturber, represented by some softened fixed potential, embedded within a gaseous medium moving with some bulk flow, be used as a standard test for current and new multi-physics codes. It concisely assesses the accuracy of both hydrodynamic and gravity solvers, used in conjunction, with a well defined solution. In particular, using results close to $\mathcal{M} = 1$, where the gaseous response is most pronounced, and the drag force is greatest, will produce interesting comparisons.

6 CONCLUSIONS

We present a suite of idealised gaseous dynamical friction simulations, using a class of Lagrangian hydrodynamical solver widely used in astrophysics, but not before tested in this manner. Specifically, the MFM solver, in *Gizmo*, with comparisons to runs using *Gadget4*, *Arepo* and *Enzo*. We find that the structure of the gravitationally induced wakes are broadly consistent with previous numerical works, and with the predictions of linear theory for a point-mass perturber, once the effects of the extended perturber are accounted for, within certain regions. In summary, we find that:

- the drag force from the overdense wake of our extended perturber fits the linear prediction for a point mass beyond $r_{\min} = 4r_s$, to within 5%
- our Mach dependent fit can convert the point mass prediction to our extended perturber results for $r_{\min} = r_s$
- we have converged with resolution, from as few as 5 cells per r_s , as well as in time, such that these results should be applicable to any equivalent setup using this solver
- the results for the different solvers are in agreement, be it the PSPH solver in *Gadget-4*, the moving-mesh MUSCL scheme in the *Arepo* code, or the PPM solver in *Enzo* (of which all codes are public)
- this result is independent of choices made in our exact setup, be it physical conditions (e.g background density/temperature) or numerical parameters (e.g time-step).

It is clear that DF is a complex problem for modern hydro solvers to treat. DF is a process that is present in astrophysical systems across a host of mass and length scales and is crucial to our understanding of the evolution of these systems. This makes DF an ideal candidate for inclusion as a standard test when developing numerical hydrodynamics methods and algorithms. It has a well-defined solution for comparison and includes both a shock with complex geometry and regions with simpler advective flows. The scale-free nature of its formulation, with the A parameter and Mach number as the defining variables, allow for straightforward comparison between numerical tests.

ACKNOWLEDGEMENTS

This work was performed using the Cambridge Service for Data Driven Discovery (CSD3), part of which is operated by the University of Cambridge Research Computing on behalf of the STFC DiRAC HPC Facility (www.dirac.ac.uk). The DiRAC component of CSD3 was funded by BEIS capital funding via STFC capital grants ST/P002307/1 and ST/R002452/1 and STFC operations grant ST/R00689X/1. DiRAC is part of the National e-Infrastructure.

We acknowledge that the results of this research have been achieved using the DECI resource ARCHER based in the UK at EPCC with support from the PRACE aisbl.

This work also used the Cirrus UK National Tier-2 HPC Service at EPCC (<http://www.cirrus.ac.uk>) funded by the University of Edinburgh and EPSRC (EP/P020267/1).

The author thankfully acknowledges RES resources provided by University of Valencia in Tirant to RES-AECT-2023-2-0026.

JO acknowledges support from grants PID2022-138855NB-C32 and CNS2022-135878 funded by MICIU/AEI/10.13039/501100011033 and European Union NextGenerationEU/PRTR.

For the purpose of open access, the author has applied a Creative Commons Attribution (CC BY) licence to any Author Accepted Manuscript version arising from this submission.

DATA AVAILABILITY

All data produced from the simulations discussed in this work are available on request.

REFERENCES

- Adhikari S., Dalal N., Clampitt J., 2016, *J. Cosmology Astropart. Phys.*, **2016**, 022
- Agertz O., et al., 2007, *MNRAS*, **380**, 963
- Antoni A., MacLeod M., Ramirez-Ruiz E., 2019, *ApJ*, **884**, 22
- Arth A., Donnert J., Steinwandel U., Böss L., Halbesma T., Pütz M., Hubber D., Dolag K., 2019, arXiv e-prints, p. [arXiv:1907.11250](https://arxiv.org/abs/1907.11250)
- Barnes J. E., Hernquist L., 1996, *ApJ*, **471**, 115
- Beckman J., Carretero C., Vazdekis A., 2008, Chinese Journal of Astronomy and Astrophysics Supplement, **8**, 77
- Beckmann R. S., Slyz A., Devriendt J., 2018, *MNRAS*, **478**, 995
- Bernal C. G., Sánchez-Salcedo F. J., 2013, *ApJ*, **775**, 72
- Bonetti M., Bortolas E., Lupi A., Dotti M., Raimundo S. I., 2020, *MNRAS*, **494**, 3053
- Bortolas E., Bonetti M., Dotti M., Lupi A., Capelo P. R., Mayer L., Sesana A., 2021, arXiv e-prints, p. [arXiv:2103.07486](https://arxiv.org/abs/2103.07486)
- Boylan-Kolchin M., Ma C.-P., Quataert E., 2008, *MNRAS*, **383**, 93
- Bryan G. L., et al., 2014, *ApJS*, **211**, 19
- Chandrasekhar S., 1943, *ApJ*, **97**, 255
- Colella P., Woodward P. R., 1984, *Journal of Computational Physics*, **54**, 174
- Daddi E., et al., 2010, *ApJ*, **714**, L118
- Donnert J. M. F., Beck A. M., Dolag K., Röttgering H. J. A., 2017, *MNRAS*, **471**, 4587
- Dosopoulou F., Antonini F., 2017, *ApJ*, **840**, 31
- Duffell P. C., 2016, *ApJS*, **226**, 2
- Duffell P. C., MacFadyen A. I., 2011, *ApJS*, **197**, 15
- El-Zant A. A., Kim W.-T., Kamionkowski M., 2004, *MNRAS*, **354**, 169
- Fujii M., Funato Y., Makino J., 2006, *PASJ*, **58**, 743
- Furlanetto S. R., Loeb A., 2002, *ApJ*, **565**, 854
- Gingold R. A., Monaghan J. J., 1977, *MNRAS*, **181**, 375
- Gonnet P., 2014, arXiv e-prints, p. [arXiv:1404.2303](https://arxiv.org/abs/1404.2303)
- Hopkins P. F., 2015, *MNRAS*, **450**, 53
- Just A., Kegel W. H., 1990, *A&A*, **232**, 447
- Just A., Khan F. M., Berczik P., Ernst A., Spurzem R., 2010, *MNRAS*, **411**, 653
- Khochfar S., Burkert A., 2001, *ApJ*, **561**, 517
- Khochfar S., Ostriker J. P., 2008, *ApJ*, **680**, 54
- Khochfar S., et al., 2011, *MNRAS*, **417**, 845
- Kim H., Kim W., 2007, *ApJ*, **665**, 432
- Kim H., Kim W.-T., 2009, *ApJ*, **703**, 1278
- Kim W.-T., El-Zant A. A., Kamionkowski M., 2005, *ApJ*, **632**, 157
- Ma L., Hopkins P. F., Ma X., Anglés-Alcázar D., Faucher-Giguère C.-A., Kelley L. Z., 2021, arXiv e-prints, p. [arXiv:2101.02727](https://arxiv.org/abs/2101.02727)
- Menon H., Wesolowski L., Zheng G., Jetley P., Kale L., Quinn T., Governato F., 2015, *Computational Astrophysics and Cosmology*, **2**, 1
- Morton B., Khochfar S., Wu Z., 2023, *MNRAS*, **518**, 4401
- Namouni F., 2010, *MNRAS*, **401**, 319
- Nelson D., et al., 2019, *Computational Astrophysics and Cosmology*, **6**, 2
- Ogiya G., Burkert A., 2016, *MNRAS*, **457**, 2164
- Ostriker E. C., 1999, *ApJ*, **513**, 252
- Park K., Bogdanović T., 2017, *ApJ*, **838**, 103
- Plummer H. C., 1911, *MNRAS*, **71**, 460
- Robaina A. R., Bell E. F., van der Wel A., Somerville R. S., Skelton R. E., McIntosh D. H., Meisenheimer K., Wolf C., 2010, *ApJ*, **719**, 844
- Sánchez-Salcedo F. J., Brandenburg A., 1999, *ApJ*, **522**, L35
- Sánchez-Salcedo F. J., Brandenburg A., 2001, *MNRAS*, **322**, 67
- Somerville R. S., Davé R., 2015, *ARA&A*, **53**, 51
- Springel V., 2005, *MNRAS*, **364**, 1105
- Springel V., 2010, *MNRAS*, **401**, 791
- Springel V., et al., 2008, *MNRAS*, **391**, 1685
- Springel V., Pakmor R., Zier O., Reinecke M., 2020, arXiv e-prints, p. [arXiv:2010.03567](https://arxiv.org/abs/2010.03567)
- Suzuguchi T., Sugimura K., Hosokawa T., Matsumoto T., 2024, *ApJ*, **966**, 7
- Tacconi L. J., et al., 2010, *Nature*, **463**, 781
- Tagawa H., Saitoh T. R., Kocsis B., 2018, *Phys. Rev. Lett.*, **120**, 261101
- Teyssandier J., Terquem C., Papaloizou J. C. B., 2012, *MNRAS*, **428**, 658
- Teyssier R., 2002, *A&A*, **385**, 337
- Thun D., Kuiper R., Schmidt F., Kley W., 2016, *A&A*, **589**, A10
- Tittle E. R., Pearce F. R., Couchman H. M. P., 2001, *ApJ*, **561**, 69
- Toyouchi D., Hosokawa T., Sugimura K., Kuiper R., 2020, *MNRAS*, **496**, 1909
- Wadsley J. W., Stadel J., Quinn T., 2004, *New Astron.*, **9**, 137
- Wadsley J. W., Keller B. W., Quinn T. R., 2017, *MNRAS*, **471**, 2357
- Weisz D., Boylan-Kolchin M., 2019, *BAAS*, **51**, 1
- Zhao H., 2004, *MNRAS*, **351**, 891

APPENDIX A: INTRINSIC FORCE VARIATION

The A parameter, which effectively sets the linearity of the numerical setup, can be varied by changing any of its dependent variables: the perturber mass, the sound speed of the background gas, and the gravitational softening scale of the perturber. Setups with the same A parameter constructed with different combinations of these parameters should produce the same results. However, there is an intrinsic error in the force produced by a given setup, effectively dictated by the inner radius, which forms the lower limit of the force integral, the mass of the perturber, and the mass of the gas particles. If we consider a scenario where the perturber does not act on the medium, then as the initial distribution of particles moves past the perturber position, the configuration of finite masses will produce variation in the net force on the perturber. This force from the unperturbed medium should be zero, but the sampling of the medium by finite mass particles leads to some variation from this value. The lower limit of the integral sets the distance of the nearest particle included in the force summation. Small lower limits lead to large contributions from the particles very close to the perturber, where the small volumes are sampled by few particles. Large r_{\min} leads to smaller variation. For a given background density and integral lower limit, the ratio of the particle mass to perturber mass M_{part}/M_p has a significant role in determining the level of intrinsic variation. The larger this ratio is, the more severe the impact of the closest particles to the perturber. Figure A1 shows the force on the central massive perturber from the glass like initial conditions. The force was calculated by direct summation of the Newtonian gravitational force between the central mass and the gas particles, excluding particles within r_{\min} of the centre. This effectively shows the uncertainty in the force for different choices of the inner radius. The specific cases shown here are for the $M_p = 2.5 \times 10^3 M_\odot$ perturber and $N = 512^3$ particles, with $L = 1, 10, 100$ kpc. The ratios of particle mass to perturber mass are 6×10^{-11} (light blue), 6×10^{-11} (orange), and 6×10^{-5} (green) respectively.

The numerical dimensionless force increases linearly with the ratio of particle mass to perturber mass, for a given background density. We can estimate the underlying uncertainty in the force from the output of a given setup. This intrinsic variation effectively limits the setups that will produce useful results, because the error can be too large to say anything meaningful about the force from the resultant wake. We must balance the need for a large box to reach large numbers of crossing times with the need to keep the number density high.

APPENDIX B: SIMULATION DATA

We are using haloes and subhaloes from the IllustrisTNG-300 simulation box (Nelson et al. 2019), at redshift $z = 0$, to assess the conditions in which simulated subhaloes are found. We select all host haloes in the mass range $10^{11} M_\odot$ to $10^{15} M_\odot$. For each host

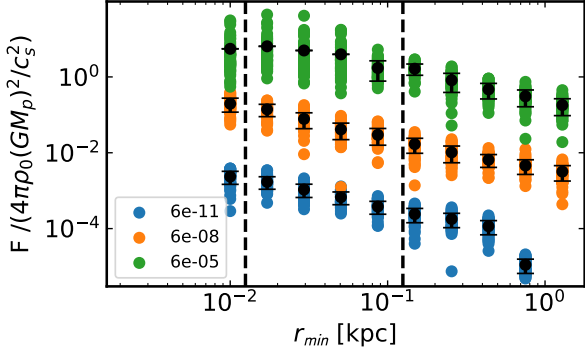


Figure A1. Force on a $M_p = 2.5 \times 10^3 M_\odot$ perturber from the initial particle distribution for setups with mass ratios of $M_{\text{particle}}/M_{\text{perturber}} = 6 \times 10^{-11}$ (light blue dots), 6×10^{-8} (orange dots), 6×10^{-5} (green dots). ICs are randomly shifted 50 times for each tested r_{min} . The coloured dots show the net dimensionless force on the perturber at the centre of the box, excluding all particles within r_{min} of the perturber. The black dots show the mean force at that r_{min} , with error bars showing the standard deviation in the forces. The variation rises significantly with particle-perturber mass ratio, and falls as r_{min} is increased. The variation shown here effectively limits the scenarios that can be run with these solvers.

in this range, we then assign a sound speed. This sound speed is calculated from the virial temperature of that halo

$$c_s = \sqrt{\frac{\gamma k_B T_{\text{vir}}}{\mu m_p}}, \quad (\text{B1})$$

where μ is the mean molecular weight of the gas, m_p is the mass of a proton. The virial temperature T_{vir} is found by assuming that the gas falling onto the virial radius transforms its kinetic energy into thermal energy. If we assume this produces an isothermal sphere, the virial temperature is given by

$$T_{\text{vir}} = \frac{1}{3} \frac{\mu m_p}{k_B} \frac{GM_{200}}{r_{200}}. \quad (\text{B2})$$

The virial mass is taken as the mass M_{200} enclosed within the radius r_{200} . This is the radius at which the average density of the enclosed material falls to two hundred times the critical density ρ_{crit} . The subhaloes associated with these hosts are then binned by their mass and this sound speed. The most massive subhalo in each host is excluded, as it is assumed to be the central object of that halo.

These subhaloes are taken as the perturbing massive objects, as they move through the extended gaseous medium of their host. The peculiar velocity of the subhalo, relative to the peculiar velocity of the host halo, defines the velocity for the calculation of the subhalo's Mach number. The radial extent of the subhalo is the equivalent to the softening scale of the Plummer potential. This is taken as the radius at which the density profile of the subhalo produces the maximum circular velocity V_{max} . The mass of the subhalo, which is the equivalent quantity to the mass of the perturber, is simply the total baryonic and dark matter mass associated to that subhalo by the halo identification algorithm.

This paper has been typeset from a $\text{\TeX}/\text{\LaTeX}$ file prepared by the author.